

DOI: 10.1002/cplu.201300435

# Synthesis and Growth Mechanism of White-Fungus-Like Nickel Sulfide Microspheres, and Their Application in Polymer Composites with Enhanced Microwave-Absorption Properties

Shuai He, Chang Lu, Guang-Sheng Wang,\* Jia-Wei Wang, Hao-Yue Guo, and Lin Guo\*<sup>[a]</sup>

White-fungus-like NiS<sub>x</sub> microspheres have been synthesized on a large scale by using a simple hydrothermal method. The influence of the reaction time and the surfactant on the final products was investigated, and the formation mechanism was discussed. The synthesized white-fungus-like NiS<sub>x</sub> microspheres were used firstly as fillers in the fabrication of NiS<sub>x</sub>/polyvinyl-

dene fluoride (PVDF) composites. Relationships between the loadings of the NiS<sub>x</sub> and wave-absorption properties of the composites were analyzed. The loss mechanisms of NiS<sub>x</sub>/PVDF with different loadings were also discussed according to their dielectric and magnetic behaviors.

## Introduction

The fabrication of microwave-absorption materials is a central issue in solving the expanding electromagnetic-interference problems caused by the rapid development of wireless communications and high-frequency circuit devices in the gigahertz range,<sup>[1]</sup> which not only influence the operation of electronic devices, but are also harmful to the health of human beings.<sup>[2]</sup>

Conventional microwave absorbents that have been widely studied in this field are as follows: 1) ferrite oxides,<sup>[3]</sup> 2) carbon,<sup>[4]</sup> 3) ceramic material,<sup>[5]</sup> including SiC, Si<sub>3</sub>N<sub>4</sub>, and their Si/C/N composites; and 4) metal material.<sup>[6]</sup> However, the densities of the above materials are usually high, which greatly limits their use in some specialized applications. In addition, for the materials (carbon nanotubes (CNTs) and graphene) with relatively low densities, the fabrication of these materials involves complex processes. Therefore, it is desirable to exploit new kinds of materials with low density, excellent wave absorption, and inexpensive fabrication cost.

Fortunately, many nanomaterials have been proven to have excellent wave-absorption properties in recent years, such as CeO<sub>2</sub>,<sup>[7]</sup> BiFeO<sub>3</sub>,<sup>[8]</sup> Fe/CNTs,<sup>[6]</sup> and CuS.<sup>[9]</sup> The subsequent challenge in this field should be utilizing these materials in fabricated materials with mechanical properties. Therefore, some-

day we can finally achieve their application, for example, in the walls of a microwave darkroom<sup>[10]</sup> or in stealth technology for aircraft.<sup>[11]</sup>

The fabrication of organic–inorganic nanocomposites seems to be a wise way to face the challenge, considering that nanocomposites have mechanical properties that nanoparticles do not; and recent studies also show that the existence of synergistic effects in organic–inorganic nanocomposites could improve their performance in many fields.<sup>[12]</sup>

Typical nanocomposites consist of a matrix and fillers. Polyvinylidene fluoride (PVDF), a semicrystalline polymer with a repeat unit of CH<sub>2</sub>–CF<sub>2</sub>, stands out amongst other polymers owing to its excellent pyro- and piezoelectric properties. It has also been widely studied as a matrix for composites with specific properties, such as a dielectric field.<sup>[13]</sup>

The NiS<sub>x</sub> nanomaterials were selected as fillers in our study owing to their interesting electrical, optical, and magnetic properties.<sup>[14]</sup> In addition, nickel sulfides can form various phases,<sup>[15]</sup> such as NiS, Ni<sub>3+x</sub>S<sub>2x</sub>, Ni<sub>3</sub>S<sub>2x</sub>, Ni<sub>7</sub>S<sub>6x</sub>, Ni<sub>3</sub>S<sub>4x</sub>, and NiS<sub>2x</sub>, and have multiple applications, including as photocatalysts for H<sub>2</sub> evolution,<sup>[16]</sup> possible transformation toughener,<sup>[17]</sup> cathode materials for rechargeable lithium batteries,<sup>[18]</sup> or as a high-boiling solvent for all-solid-state lithium secondary batteries.<sup>[19]</sup> Furthermore, Du's group introduced the application of iron/nickel sulfide filled carbon nanotubes and their microwave-absorbing properties,<sup>[20]</sup> with a maximum reflection loss of –29.58 dB. However, to the best of our knowledge, the microwave-absorbing properties of pure NiS<sub>x</sub> or its related inorganic–organic composite have not previously been reported.

However, in spite of the success in the synthesis of various morphologies,<sup>[21]</sup> including nanorods, triangular nanoprisms, hollow spheres, thin films, nanochains, and layer-rolled structures, the preparation of uniform hierarchical hollow structures of nickel sulfides still remains a significant challenge.

[a] S. He,<sup>†</sup> C. Lu,<sup>†</sup> Dr. G.-S. Wang, J.-W. Wang, H.-Y. Guo, Prof. L. Guo  
Key Laboratory of Bio-Inspired Smart Interfacial Science and Technology of  
Ministry of Education  
Beijing Key Laboratory of Bio-Inspired Energy Materials  
and Devices, School of Chemistry and Environment  
Beihang University, Beijing 100191 (P. R. China)  
E-mail: wanggsh@buaa.edu.cn  
guolin@buaa.edu.cn

<sup>†</sup> These authors contributed equally to this study.

 Supporting information for this article is available on the WWW under  
<http://dx.doi.org/10.1002/cplu.201300435>.

In this study, we introduce a one-step thermal process to synthesize a nickel sulfide hierarchical hollow structure (white-fungus-like nanostructure), which has never been reported as far as we know. Details on its dielectric properties and growth mechanism are discussed. We also prepared  $\text{NiS}_x/\text{PVDF}$  nanocomposites through a hot-press method. The wave-absorption properties of these nanocomposites were also investigated and explained.

## Results and Discussion

### Characteristics of the synthesized $\text{NiS}_x$ white-fungus-like microspheres

Scanning electron microscopy (SEM) images of the as-prepared nickel sulfide are shown in Figure 1a–c. According to Figure 1a, the synthesized nickel sulfide products are microspheres with

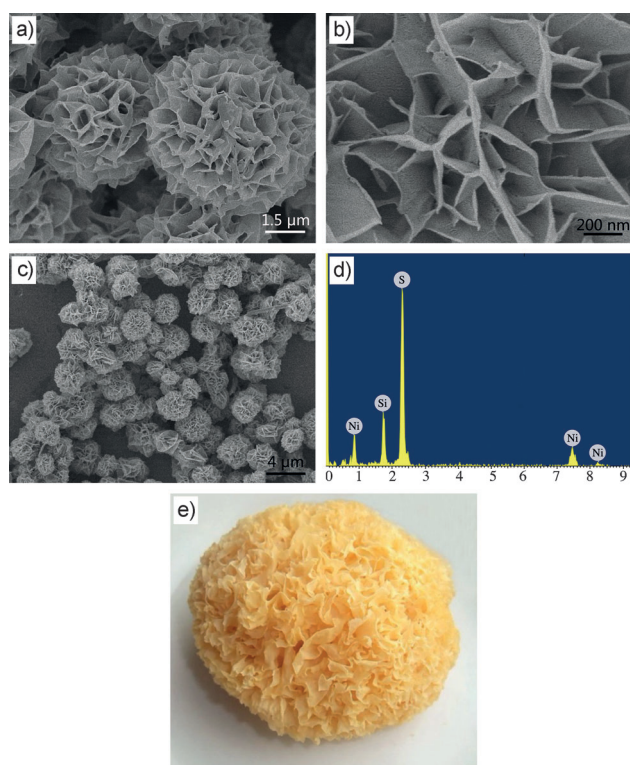


**Figure 1.** (a, b, c) SEM images of synthesized nickel sulfide nanomaterials with different magnification times; (d) EDS results of nickel sulfide and (e) image of white fungus.

diameters of around  $4\ \mu\text{m}$ . Figure 1b shows the amplified image of one microsphere, which indicates the existence of nanostructures in its surface. In addition, the synthesized products appear to possess superior dispersibility, as showed in the low-magnification SEM image (Figure 1c). Interestingly, the nickel sulfide microsphere with a suprananostructure that we synthesized is consistent with the structure of white fungus (shown in Figure 1e): they are both spherical, and both their structures consist of flexible sheets. It is really amazing that chemistry and biology could compose identical structures on

different scales. Therefore, we would like to name the synthesized  $\text{NiS}_x$  nanomaterial as white-fungus-like microspheres (abbreviated as WFMS).

The energy-dispersive X-ray spectroscopy (EDS) results shown in Figure 1d indicate that the nanoparticles contain the elemental sulfur and nickel with an atomic ratio close to 2:1. Elemental copper also appeared in the EDS spectrum, which possibly comes from the TEM grid.

The crystal phase of the product was identified by powder XRD (as shown in Figure 2). The results clearly show that most of the peaks can be attributed to  $\text{NiS}_2$  (JCPDS no. 11-0099).

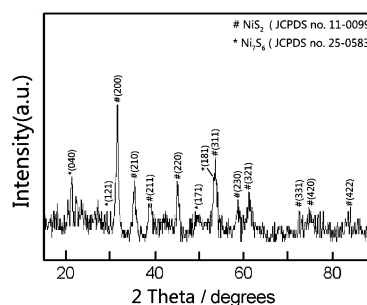


**Figure 2.** XRD results of  $\text{NiS}_x$  WFMS.

However, the XRD results also show that the synthesized  $\text{NiS}_2$  nanoparticles are poorly crystallized, and some peaks could also be attributed to other phases of nickel sulfide, such as  $\text{Ni}_7\text{S}_6$ .

Figure 3a shows a low-magnification TEM image of the synthesized  $\text{NiS}_x$  WFMS, which can be clearly identified as a micro-

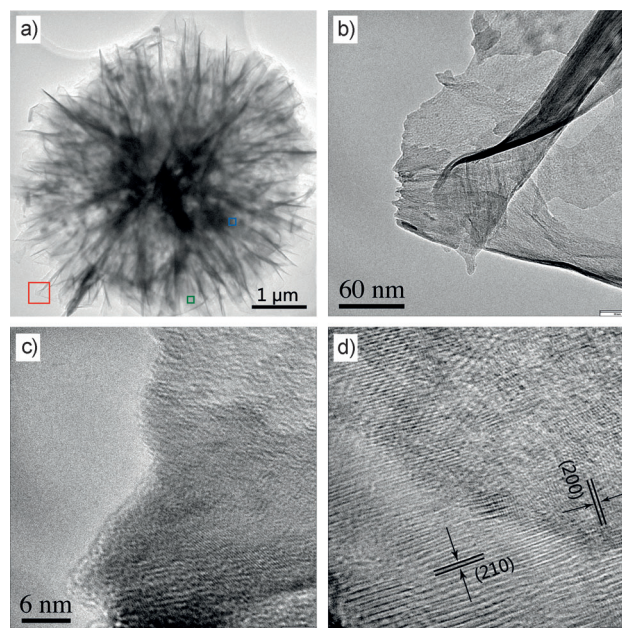


**Figure 3.** (a) Low-magnification TEM image of the synthesized  $\text{NiS}_x$  WFMS. (b) Magnified TEM images taken from (a); (c, d) HRTEM images taken from different areas.

sphere. Figure 3b–d are magnified TEM images taken from Figure 3a. Figure 3b shows that at the periphery of this microsphere, the sheet that consists of the microsphere is extremely thin, which suggests a relatively large specific surface area (in fact, the BET surface area of the synthesized  $\text{NiS}_x$  microspheres is  $22 \text{ m}^2 \text{ g}^{-1}$ ). Figure 3c and d are HRTEM images that are taken from different areas: Figure 3c is taken from the edge, whereas Figure 3d is taken from the central part (the sheets are too thick to enable a clear image to be obtained in an area closer to the core). As these two images show, in the central part, the crystal lattices can easily be recognized. However, in the part close to the periphery, the crystal lattices are very indistinct, which indicates a poorer crystallization process, which corresponds well with the XRD results. In fact, during our TEM analysis, we have observed several different microspheres; they all show the same crystallization situation as discussed above. The crystal lattices that appear in Figure 3d can be indexed to (210) and (200) from  $\text{NiS}_2$  materials, which are very consistent with the XRD results. Therefore, these analytical data agree well with our experimental results.

### The controlled synthesis of the nickel sulfide WFMS

To further reveal the growth mechanism of the nickel sulfide WFMS, the products were collected at certain reaction-time intervals for SEM observation. Figure 4 shows representative SEM images of the products prepared at  $120^\circ\text{C}$  after 4, 8, 24, and 48 hours. It is worth mentioning that the same reaction was also repeated with a time interval of 3 hours. However, no

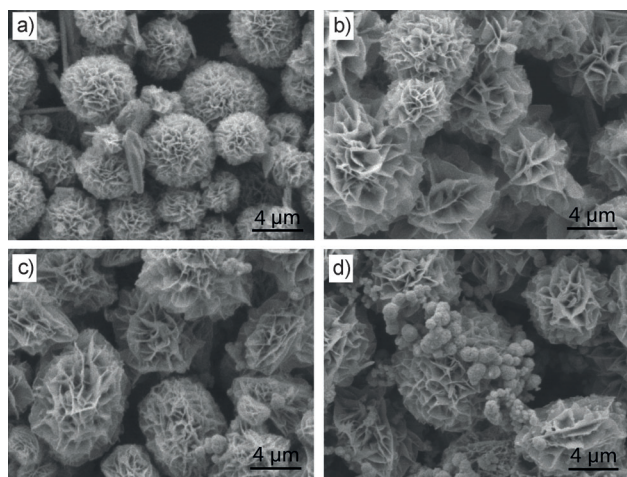


**Figure 4.** SEM images of the synthesized nickel sulfide WFMS at different reaction time intervals: (a) 4, (b) 8, (c) 24, and (d) 48 h.

product was acquired. Therefore, this reaction is considered to start slowly with a preparation period of as long as 3 hours. The standard nickel sulfide WFMS firstly appeared when the reaction time was extended to 4 hours, although their monodispersity was lower than those synthesized in 6 hours. Therefore, after a preparation period, nickel sulfide WFMS grow really fast.

With the increase of reaction time, the size of the nickel sulfide WFMS also increases (although is not very apparent). When the reaction time was prolonged to 24 hours (Figure 4c), the synthesized nickel sulfide WFMS transformed into spheroidlike structures. And after 48 hours, some little nanoparticles appeared as shown in Figure 4d. But major products were still nickel sulfide WFMS, which indicated a good stability of the nickel sulfide WFMS in the reaction system, which is very important in industrial production.

The amount of cetyltrimethylammonium bromide (CTAB; served as the surface active agent) that was added in the system also proved to have a very strong influence on the structures of the synthesized nickel sulfide microparticles. Figure 5 shows the SEM images of the nickel sulfide WFMS synthesized with different amounts of CTAB. These images show that all of the synthesized nickel sulfide WFMS have flowerlike structures when the amount of CTAB is in the range of

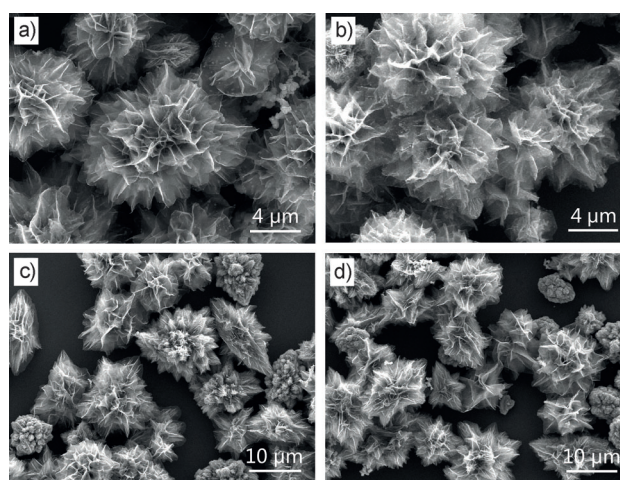
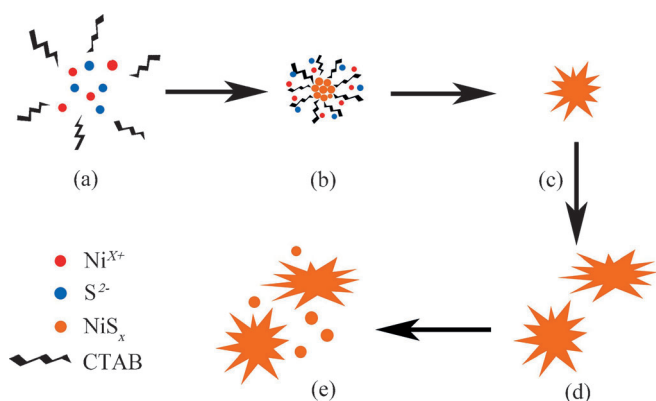


**Figure 5.** SEM images of the synthesized nickel sulfide WFMS with different amounts of CTAB: (a) 0.416, (b) 0.520, (c) 0.832, and (d) 0.936 g.

0.416 to 0.936 g. However, the difference between those structures also stands out. When the amount of CTAB is decreased, the nickel sulfide structures consist of thinner nanosheets (shown in Figure 5a,b). On the contrary, the structures become spheroidlike with many clear sharp points if the amount of CTAB is increased to 0.832 g or higher. The maximum amount of CTAB we added was 0.936 g, for it takes more effort to dissolve the increased amount of CTAB in 80 mL *N,N*-dimethylformamide (DMF) only through magnetic stirring. Therefore, both increasing or decreasing the amount of surfactant have a clear influence on the structures and the above-mentioned nickel sulfide WFMS can only be synthesized with a certain amount of CTAB (0.728 g). In conclusion, the growth mechanism is quite simple. Under the influence of CTAB, S is reduced to  $\text{S}^{2-}$ , and finally forms the nickel sulfide WFMS within 4 hours. If we prolong the reaction time, the  $\text{NiS}_x$  WFMS continue to grow. However, there will be some changes in their structures. From the reaction conditions mentioned above, we give the growth mechanism of the nickel sulfide WFMS in Scheme 1.



Scheme 1. Growth mechanism of nickel sulfide WFMS.

### Wave-absorption properties

The reflection-loss (RL) coefficients of these materials were calculated by using the measured relative complex permittivity and permeability values. According to transmission line theory, the RL coefficient (in dB) of the electromagnetic wave (normal incidence) at the surface of a single-layer material backed by a perfect conductor at a given frequency and layer thickness can be defined by Equations (1) and (2).<sup>[22]</sup>

$$Z_{in} = \sqrt{\frac{\mu_r}{\epsilon_r} \tan h \left[ j \left( \frac{2f\pi d}{c} \right) \sqrt{\mu_r \epsilon_r} \right]} \quad (1)$$

$$R = 20 \log \left| \frac{Z_{in} - 1}{Z_{in} + 1} \right| \quad (2)$$

in which  $Z_{in}$  is the input impedance of the absorber,  $\mu_r$  is the relative complex permeability (due to lack of magnetic properties, the  $\mu_r$  values of NiS<sub>x</sub> are treated as 1),  $\epsilon_r$  is the complex permittivity,  $f$  is the frequency of the microwaves,  $d$  is the thickness of the absorber,  $h$  is Planck's constant, and  $c$  is the velocity of light. Based on the above equations, the reflection losses of different samples were all calculated and are shown in Figures 6 and 7.

Figure 6a,b,c show that the RLs of NiS<sub>x</sub>/paraffin with low loadings (5 to 20 wt%) are very poor. Only when the loading is raised to 30 wt%, is the microwave absorption of NiS<sub>x</sub>/paraffin also enhanced and several sharp peaks can be noted in the frequency range of 8–10 GHz (shown in Figure 6d). Therefore, the relationship between the wave-absorption properties of NiS<sub>x</sub>/paraffin and the loading of NiS<sub>x</sub> is quite simple: higher loading, stronger absorption.

Figure 7 shows a comparison of calculated RL curves in the frequency range of 2–18 GHz for the NiS<sub>x</sub>/PVDF composites with different thicknesses and different loadings. The results clearly demonstrate that the fabrication of a NiS<sub>x</sub>/PVDF composite could greatly enhance the wave-absorption properties, especially when the loading is relatively low. As Figure 7a,b shows, several strong peaks can be found in the frequency range of 8–10 GHz. When the loading of NiS<sub>x</sub> is raised to 20 wt%, these absorption peaks in the range of 8–10 GHz dis-

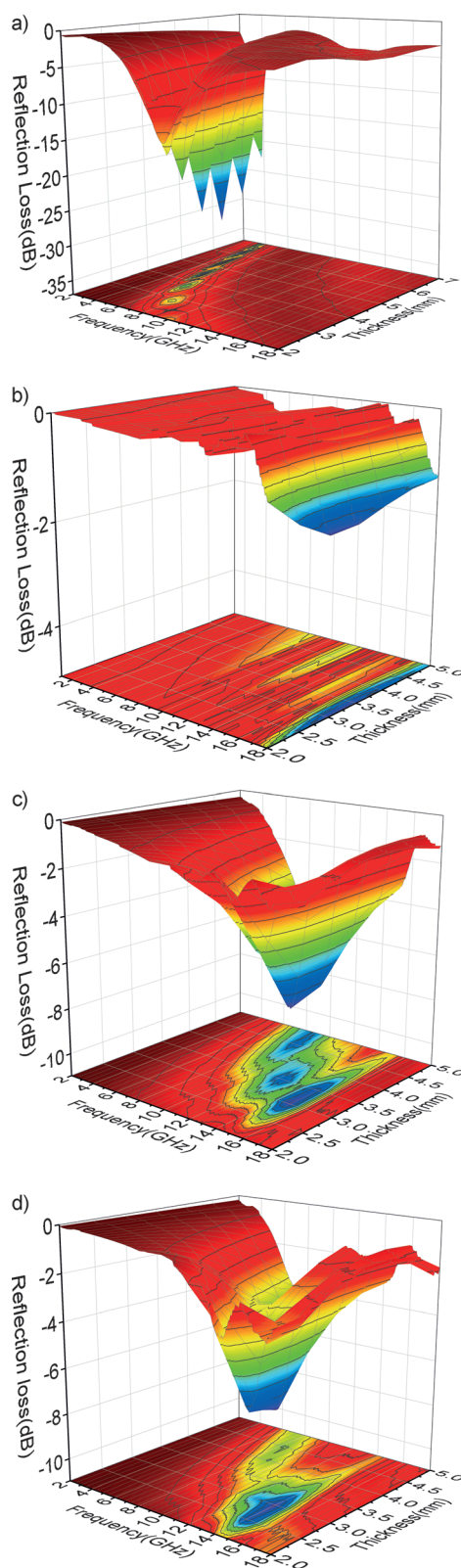
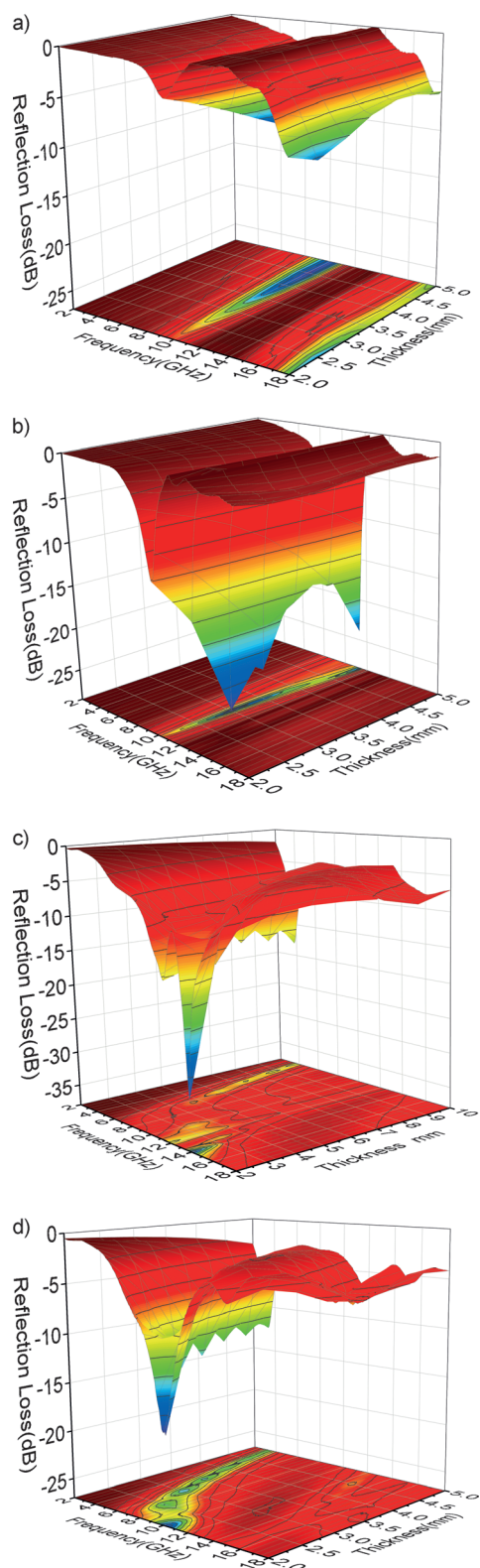


Figure 6. Wave-absorption properties of NiS<sub>x</sub>/paraffin composites with different NiS<sub>x</sub> loadings calculated based on relative complex permittivity and permeability: (a) 5, (b) 10, (c) 20, and (d) 30 wt%.

appear, while others emerge in both the low- and high-frequency regions (shown in Figure 7c). As a consequence, the



**Figure 7.** The wave-absorption properties of  $\text{NiS}_x/\text{PVDF}$  composites with different  $\text{NiS}_x$  loadings calculated based on relative complex permittivity and permeability: (a) 5, (b) 10, (c) 20, and (d) 30 wt %.

absorption range increases: the reflection loss over the whole frequency range is almost lower than  $-5$  dB. In addition, even when the thickness of the sample is as thin as 2 or 2.5 mm,

the 20 wt% loading composite still has sharp absorption peaks, much better than lower loading samples with the same thickness. Therefore, when the loading increases to 20 wt%, the wave-absorption properties of the composite can still be enhanced.

However, we can hardly get samples with better microwave-absorption properties by continually increasing the loading of  $\text{NiS}_x$  as shown in Figure 7d. In fact, the wave-absorption ability of the 30 wt% sample seems to be even worse than that of the 20 wt% loading sample, considering that the minimum RL of the 30 wt% sample can reach  $-35$  dB, while the latter can only reach  $-20$  dB with the same thickness. Hence, different to the  $\text{NiS}_x/\text{paraffin}$  composite, the relationship between the wave-absorption properties and the loadings in the  $\text{NiS}_x/\text{PVDF}$  composite tends to be more complex: the wave-absorption intensity increases along with loadings when the loading is relatively low, nevertheless, when the loading is increased to an established value, the wave-absorption intensity will reach a maximum value and begin to decrease.

By comparing the RL values between these two samples, we find the enhancement in the wave absorption of the  $\text{NiS}_x/\text{PVDF}$  composite is more evident when the loading is low. Even by taking RL values of pure PVDF samples into consideration (see Figure S1), the wave-absorption properties of  $\text{NiS}_x/\text{PVDF}$  are much better than those of  $\text{NiS}_x/\text{paraffin}$ . What is more, the RL value of  $\text{NiS}_x/\text{PVDF}$  is lower than the numerical addition of  $\text{NiS}_x/\text{paraffin}$  and pure PVDF, which indicates that the enhanced wave-absorption properties of  $\text{NiS}_x/\text{PVDF}$  are not just the physical addition of  $\text{NiS}_x$  and PVDF.

The reflection and attenuation properties of the  $\text{NiS}_x$  composite absorber depend on the dielectric loss and magnetic loss. Therefore, to investigate the possible mechanisms of the microwave absorption of different samples, we independently display their complex permittivity and complex permeability in Figures 8 and 9.

Figure 8a,b shows that the fabrication of the  $\text{NiS}_x/\text{PVDF}$  composites improves the dielectric properties of low-loading samples (10 and 20 wt%, respectively). Both the real-part and imaginary-part permittivity at those loadings are much higher in the  $\text{NiS}_x/\text{PVDF}$  composite than in the  $\text{NiS}_x/\text{paraffin}$  composite, which results in a greatly enhanced wave-absorption property. However, the complex permittivity of the  $\text{NiS}_x/\text{paraffin}$  sample could be surprisingly improved by increasing the loading to 30 wt% (shown in Figure 8c,d), whereas the same improvement did not appear in the  $\text{NiS}_x/\text{PVDF}$  composite. Consequently, even though the complex permittivity of  $\text{NiS}_x/\text{PVDF}$  is still higher than that of  $\text{NiS}_x/\text{paraffin}$ , the distinction is not strong enough to make a clear difference in their reflection loss.

Reflection-loss behaviors of materials depend on their loss mechanisms, which are determined by their nature, shape, size, and microstructures.<sup>[23]</sup> In the present study, there are several mechanisms that can account for the efficient microwave-absorption properties of the  $\text{NiS}_x/\text{PVDF}$  composite.

First, the reflection loss is likely caused by Debye dipolar relaxation, which is a crucial mechanism for an inorganic–organic composite to absorb microwaves, as we mentioned

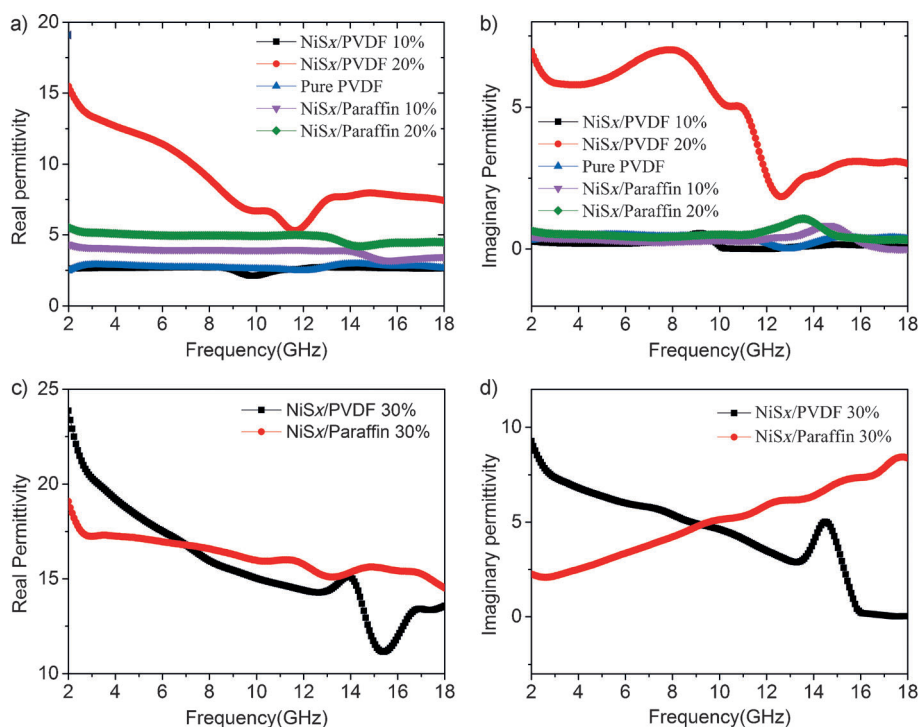


**Figure 8.** Measured frequency dependence of (a,c) real parts and (b,d) imaginary parts of complex permittivity of different samples.

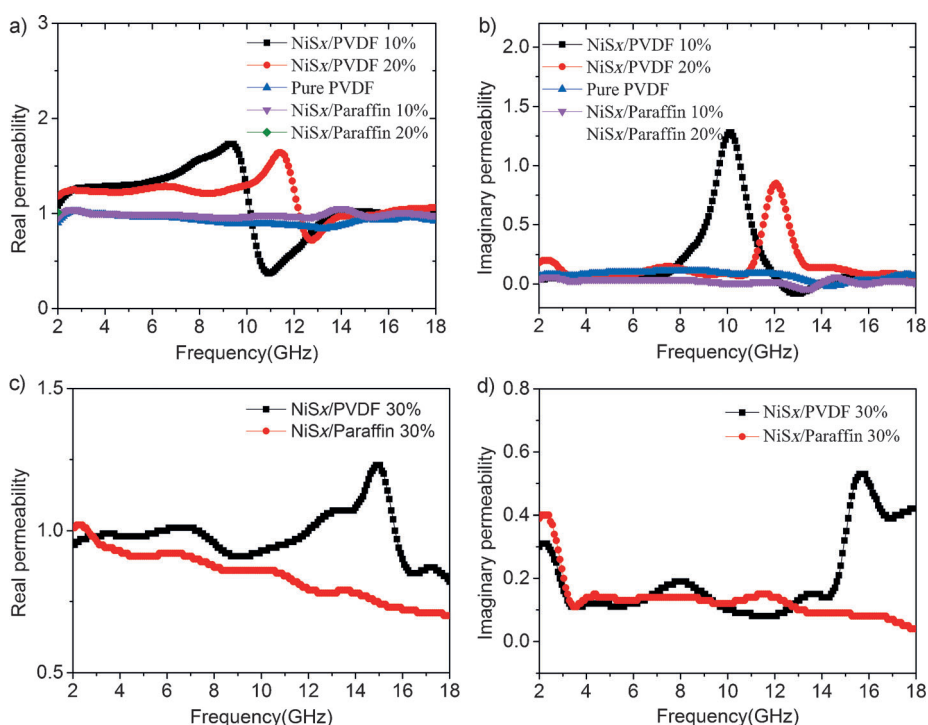


**Figure 9.** Measured frequency dependence of (a,c) real parts and (b,d) imaginary parts of complex permeability of different samples.

before.<sup>[24,25]</sup> As we know, the relaxation process is usually caused by the delay in molecular polarization with respect to

the existence of interfaces gives rise to interfacial polarization (Maxwell–Wagner effect).<sup>[25]</sup> However, according to the free-

changing electric field in a dielectric medium. Figure S2 shows the  $\epsilon' - \epsilon''$  curve of the different samples. If the Debye relaxation process accounts for dielectric loss behavior, the relationship between  $\epsilon'$  and  $\epsilon''$  can be deduced as shown in Equation (3;  $\epsilon_s$  is static permittivity):

$$\left(\epsilon' - \frac{\epsilon_s + \epsilon_\infty}{2}\right)^2 + (\epsilon'')^2 = \left(\frac{\epsilon_s - \epsilon_\infty}{2}\right)^2 \quad (3)$$

Thus, the plot of  $\epsilon'$  versus  $\epsilon''$  would be a single semicircle, generally denoted as the Cole–Cole semicircle.

As shown in Figure S2g, an obvious Cole–Cole semicircle was found in the  $\epsilon' - \epsilon''$  curves of PVDF with a loading of 10 wt%, which indicate that the Debye relaxation process may be mainly responsible for its dielectric loss behavior. In addition, low-loading NiS<sub>x</sub>/paraffin samples (10 and 20 wt%) also have one Cole–Cole semicircle in their  $\epsilon' - \epsilon''$  curves (shown in Figure S2c,d), which shows that their dielectric loss may also result from a Debye relaxation process.

After the addition of the NiS<sub>x</sub> nanomaterial, more semicircles could be found, representing more loss mechanisms. Additionally, more semicircles also appear in the 30 wt% loading NiS<sub>x</sub>/paraffin composite (seen in Figure S2a,c,e,f). Hence, in those samples, the dielectric loss behavior is more complex, which results in stronger wave-absorption behaviors.

Other kinds of loss mechanisms are Maxwell–Wagner relaxation and electron polarization. The former behavior appears in heterogeneous media owing to the accumulation of charges at the interfaces and the formation of large dipoles on particles or clusters, whereas in composites,

electron theory  $\epsilon'' \propto \sigma / 2\pi\epsilon_0 f$  ( $\sigma$  is the electrical conductivity), increased conductivity of a composite results in stronger dielectric loss.  $\text{NiS}_x$  has relatively good electrical conductivity, and the addition of  $\text{NiS}_x$  should considerably enhance the conductivity of the fabricated  $\text{NiS}_x/\text{PVDF}$  composite, and result in better wave-absorption properties.

Besides the dielectric properties, the enhancements in the magnetic properties of  $\text{NiS}_x/\text{PVDF}$  also have positive effects on their wave-absorption properties. From Figure 9, we can easily see that the fabrication of  $\text{NiS}_x/\text{PVDF}$  composites also gives rise to their magnetic properties: unlike the permeability curves of the  $\text{NiS}_x/\text{paraffin}$  composites, there are some strong peaks in those of  $\text{NiS}_x/\text{PVDF}$ . Interestingly, those peaks happen to correspond to the peak valley of permittivity curves of the  $\text{NiS}_x/\text{PVDF}$  composite (shown in Figure 8), which indicates that the electric energy and magnetic energy convert to each other at those specified frequencies. At those frequencies with valleys and peaks, the RLs also prove to be very strong (shown in Figure 7). For example, the peak in the permeability curves of the  $\text{NiS}_x/\text{PVDF}$  sample with a loading of 10 wt% appears at 10 GHz, whereas the strong wave-absorption peak also appears at the same frequency area. For the 20 wt% loading sample, the frequency is around 11 GHz, and so forth. In summary, strong absorption behaviors appear when the electromagnetism-converting behavior is noticeable, and because the electromagnetism-converting process in the  $\text{NiS}_x/\text{PVDF}$  composite is easier to achieve, the wave-absorption of  $\text{NiS}_x/\text{PVDF}$  is stronger.

## Conclusion

In summary, white-fungus-like  $\text{NiS}_x$  microspheres have been synthesized on a large scale by a simple hydrothermal method. The amount of surfactant has a great effect on the final product, and the reaction time is a key factor for the final morphology. The influence of the loadings of synthesized  $\text{NiS}_x$  on their wave-absorption properties was carefully discussed. Our results show that the  $\text{NiS}_x/\text{PVDF}$  composite with relatively low filler content (5 or 10 wt%) possesses much better microwave-absorption properties than the  $\text{NiS}_x/\text{paraffin}$  composite. Finally, loss mechanisms of  $\text{NiS}_x/\text{PVDF}$  with different loadings were also discussed and depended on their dielectric and magnetic behaviors. By combining the influence of permittivity and permeability, the wave-absorption mechanisms of the  $\text{NiS}_x/\text{PVDF}$  composite can be clearly explained.

## Experimental Section

### Materials

Nickel nitrate hexahydrate (Tianjing Jinke Refined Chemical Engineering Institute, 500 g), cetyltrimethyl ammonium bromide (Beijing chemical factory, 100 g), DMF (Beijing chemical factory, 500 mL), ethanol (Beijing chemical factory, 500 mL), elemental sulfur (Beijing chemical factory, 500 mL), and deionized water (homemade).

### Preparation of nickel sulfide WFNS

All the reagents (analytical-grade purity) were utilized without any further purification. Typically, nickel sulfide was synthesized by the reaction of  $\text{Ni}(\text{NO}_3)_2 \cdot 6\text{H}_2\text{O}$  and sulfur powder in DMF.  $\text{Ni}(\text{NO}_3)_2 \cdot 4.5\text{H}_2\text{O}$  (0.3462 g), CTAB (0.728 g), and sulfur powder (0.0768 g) were added to DMF (80 mL) under strong magnetic stirring to form a homogeneous solution. Then the prepared solution was transferred into a 100 mL Teflon-lined stainless-steel autoclave, sealed and maintained at 120 °C for 6 h. After being cooled to room temperature, the resulting solid product was filtered, washed with distilled water to remove possible remnant in the final products, and finally dried in air at 100 °C for 24 h.

### Measurement of the microwave absorption of nickel sulfide WFNS

To measure the microwave-absorption properties of pure nickel sulfide WFNS, the specimen was prepared by uniformly mixing the nickel sulfide materials in a paraffin matrix, which is transparent to microwave waves, and pressing the mixture into a cylindrical compact ( $\Phi_{\text{out}} = 7.00$  mm and  $\Phi_{\text{in}} = 3.04$  mm). The relative permittivity ( $\epsilon$ ) values were measured in the 2–18 GHz range with a coaxial wire method by an Anritsu 37269D network analyzer.

### Preparation of nickel sulfide/PVDF nanocomposites

The desired amount of nickel sulfide was first ultrasonically dispersed in DMF (30 mL) for 1 h. Then, PVDF was added into the suspension. After stirring at room temperature and ultrasonication for another 1 h, the mixture was poured onto a glass plate to form a thin film, and dried at 80 °C for 24 h. The samples for testing were also compacted into a cylindrical compact ( $\Phi_{\text{out}} = 7.00$  mm and  $\Phi_{\text{in}} = 3.04$  mm) by hot pressing at 200 °C.

### Characterization

The X-ray diffraction (XRD) pattern of the nickel sulfide product was performed on a Rigaku, Dmax2200 diffractometer equipped with a  $\text{Cu}_{\text{K}\alpha}$  radiation source ( $\lambda = 1.54180$  Å) for the structural determination. The scanning rate was 4° per minute with  $2\theta$  ranging from 20 to 70°. Further microstructural analyses were performed by using a Hitachi S4800 cold field emission scanning electron microscope (CFESEM) and high-resolution transmission electron microscopy (HRTEM) (JEOL 2100F) using an accelerating voltage of 200 kV. In brief, TEM samples were prepared by diluting the resulting solution with alcohol by ultrasonic treatment, and dropping it onto a holey carbon film supported on a copper grid, and drying the dropped sample in air. The relative permittivity  $\epsilon$  values were measured in the 2–18 GHz range with the coaxial wire method using an Anritsu 37269D network analyzer at room temperature. Specific surface areas were measured at 77 K by Brunauer–Emmett–Teller (BET) nitrogen adsorption–desorption analysis (NOVA 2200e, Quantachrome, USA).

### Acknowledgements

*This project was financially supported by the National Basic Research Program of China (no. 2010CB934700) and the National Natural Science Foundation of China (nos. 51102223, 50725208, and 51132002).*

**Keywords:** absorption · organic–inorganic hybrid composites · nanostructures · nickel · polymers

- [1] M. Zhou, X. Zhang, J. Wei, S. Zhao, L. Wang, B. Feng, *J. Phys. Chem. C* **2011**, *115*, 1398–1402.
- [2] S. M. Abbas, A. K. Dixit, R. Chatterjee, T. C. Goel, *J. Magn. Magn. Mater.* **2007**, *309*, 20–24.
- [3] V. G. Harris, *IEEE T. Magn.* **2012**, *48*, 1075–1104.
- [4] a) H. Hu, Z. Zhao, Q. Zhou, Y. Gogotsi, J. Qiu, *Carbon* **2012**, *50*, 3267–3273; b) M. Arjmand, M. Mahmoodi, G. A. Gelves, S. Park, U. Sundararaj, *Carbon* **2011**, *49*, 3430–3440.
- [5] a) D.-L. Zhao, F. Luo, W.-C. Zhou, *J. Alloys Compd.* **2010**, *490*, 190–194; b) F. Ye, L. Zhang, X. Yin, X. Zuo, Y. Liu, L. Cheng, *J. Eur. Ceram. Soc.* **2012**, *32*, 4025–4029; c) D. L. Zhao, H. S. Zhao, W. C. Zhou, *Physica E* **2001**, *9*, 679–685.
- [6] R. C. Che, L. M. Peng, X. F. Duan, Q. Chen, X. L. Liang, *Adv. Mater.* **2004**, *16*, 401–405.
- [7] H. Wu, L. Wang, Y. Wang, S. Guo, *Appl. Surf. Sci.* **2012**, *258*, 10047–10052.
- [8] Z.-L. Hou, H.-F. Zhou, L.-B. Kong, H.-B. Jin, X. Qi, M.-S. Cao, *Mater. Lett.* **2012**, *84*, 110–113.
- [9] S. He, G.-S. Wang, C. Lu, X. Luo, B. Wen, L. Guo, M.-S. Cao, *ChemPlusChem* **2013**, *78*, 250–258.
- [10] C. Burda, X. B. Chen, R. Narayanan, M. A. El-Sayed, *Chem. Rev.* **2005**, *105*, 1025–1102.
- [11] C. H. Peng, C. C. Hwang, J. Wan, J. S. Tsai, S. Y. Chen, *Mater. Sci. Eng. B* **2005**, *117*, 27–36.
- [12] Z.-A. Hu, Y.-L. Xie, Y.-X. Wang, L.-P. Mo, Y.-Y. Yang, Z. Y. Zhang, *Mater. Chem. Phys.* **2009**, *114*, 990–995.
- [13] a) V. K. Thakur, G. Ding, J. Ma, P. S. Lee, X. Lu, *Adv. Mater.* **2012**, *24*, 4071–4096; b) G.-S. Wang, Y. Deng, Y. Xiang, L. Guo, *Adv. Funct. Mater.* **2008**, *18*, 2584–2592.
- [14] a) R. L. Kautz, M. W. Keller, J. M. Martinis, *Phys. Rev. B* **2000**, *62*, 15888–15902; b) G. Krill, M. F. Lapierre, C. Robert, F. Gautier, G. Czjzek, J. Fink, H. Schmidt, *J. Phys. C: Solid State Phys.* **1976**, *9*, 761–762.
- [15] a) B. Zhang, X. C. Ye, W. Dai, W. Y. Hou, Y. Xie, *Chem. Eur. J.* **2006**, *12*, 2337–2342; b) F. Cao, R. Liu, L. Zhou, S. Song, Y. Lei, W. Shi, F. Zhao, H. Zhang, *J. Mater. Chem.* **2010**, *20*, 1078–1085; c) A. Ghezelbash, B. A. Korgel, *Langmuir* **2005**, *21*, 9451–9456; d) L. Wang, Y. Zhu, H. Li, Q. Li, Y. Qian, *J. Solid State Chem.* **2010**, *183*, 223–227.
- [16] W. Zhang, Y. Wang, Z. Wang, Z. Zhong, R. Xu, *Chem. Commun.* **2010**, *46*, 7631–7633.
- [17] J. Grau, M. Akinc, *J. Am. Ceram. Soc.* **1997**, *80*, 941–951.
- [18] a) X. J. Liu, Z. Z. Xu, H. J. Ahn, S. K. Lyu, I. S. Ahn, *Powder Technol.* **2012**, *229*, 24–29; b) S. C. Han, H. S. Kim, M. S. Song, J. H. Kim, H. J. Ahn, J. Y. Lee, *J. Alloys Compd.* **2003**, *351*, 273–278.
- [19] K. Aso, H. Kitaura, A. Hayashi, M. Tatsumisago, *J. Mater. Chem.* **2011**, *21*, 2987–2990.
- [20] Q. Su, J. Li, G. Zhong, G. Du, B. Xu, *J. Phys. Chem. C* **2011**, *115*, 1838–1842.
- [21] a) Y. Wang, Q. Zhu, L. Tao, X. Su, *J. Mater. Chem.* **2011**, *21*, 9248–9254; b) T. Zhu, Z. Wang, S. Ding, J. S. Chen, X. W. Lou, *RSC Adv.* **2011**, *1*, 397–400; c) H. Pang, Q. Lu, Y. Lia, F. Gao, *Chem. Commun.* **2009**, 7542–7544.
- [22] M.-S. Cao, X.-L. Shi, X.-Y. Fang, H.-B. Jin, Z.-L. Hou, W. Zhou, Y.-J. Chen, *Appl. Phys. Lett.* **2007**, *91*, 203110.
- [23] a) G. Wang, Z. Gao, S. Tang, C. Chen, F. Duan, S. Zhao, S. Lin, Y. Feng, L. Zhou, Y. Qin, *ACS Nano* **2012**, *6*, 11009–11017; b) X. F. Zhang, X. L. Dong, H. Huang, Y. Y. Liu, W. N. Wang, X. G. Zhu, B. Lv, J. P. Lei, C. G. Lee, *Appl. Phys. Lett.* **2006**, *89*, 053115.
- [24] Z. D. Chen, G.-S. Wang, S. He, L. Guo, M.-S. Cao, *J. Mater. Chem. A* **2013**, *1*, 5996–6003.
- [25] a) J. K. Nelson, J. C. Fothergill, *Nanotechnology* **2004**, *15*, 586–595; b) N. Ortega, A. Kumar, R. S. Katiyar, C. Rinaldi, *J. Mater. Sci.* **2009**, *44*, 5127–5142; c) P. K. Mandal, A. Lapanik, R. Wipf, B. Stuehn, W. Haase, *Appl. Phys. Lett.* **2012**, *100*, 073112.

Received: December 23, 2013

Published online on February 13, 2014